VOLUME 53 JOURNAL OF PHYSICAL OCEANOGRAPHY MAY 2023

Observational Constraints on the Submesoscale Sea Surface Height Variance of Balanced Motion

CHARLY DE MAREZ,[a] JÖRN CALLIES,[a] BRUCE HAINES,[c] DANIELA RODRIGUEZ-CHAVEZ,[a,b] AND JINBO WANG[c]

[a] *California Institute of Technology, Pasadena, California*
[b] *Cornell University, Ithaca, New York*
[c] *Jet Propulsion Laboratory, California Institute of Technology, Pasadena, California*

(Manuscript received 12 September 2022, in final form 30 January 2023, accepted 3 February 2023)

ABSTRACT: A combination of in situ and remotely sensed observations are used to constrain the imprint of submesoscale turbulence in the sea surface height (SSH) field. The distribution of SSH variance across frequencies and wavenumbers is estimated by comparing an empirical model spectrum to two sets of observations. First, submesoscale SSH variance is constrained using a pair of GPS buoys spaced at about 10 km. From these data, one can estimate frequency spectra not only of SSH variance but also of the variance in the SSH difference between the buoys. The ratio between these two spectral estimates is sensitive to how much SSH variance is present in the submesoscale range and thus constrains the spectral roll-off of SSH variance in wavenumber space. Second, a combination of moored current meters and nadir altimetry is used to obtain an independent constraint. This constraint is enabled by geostrophy and the nonseparability of the wavenumber–frequency spectrum of SSH variance revealed by the GPS data. The frequency spectra of kinetic energy and SSH variance follow different power laws, and the difference constrains the spectral content in wavenumber space, allowing for a constraint without the need to actually resolve the submesoscales in space. In all four locations studied, spanning the midlatitude and subtropical ocean, these constraints indicate that the wavenumber spectral roll-off of submesoscale SSH variance is between about k^{-4} and k^{-5}, where k is the wavenumber. These estimates are consistent with previous observations, model results, and theoretical predictions. They provide for a strong prior for the interpretation of upcoming high-resolution satellite data.

KEYWORDS: Mesoscale processes; Turbulence; In situ oceanic observations; Remote sensing; Satellite observations

1. Introduction

Oceanic currents with horizontal scales smaller than 100 km are a major part of the oceanic circulation. They include surface and subsurface submesoscale currents with horizontal scales $\lesssim 10$ km, organized into vortices, filaments, and fronts. These structures are thought to play a key role in the ocean's primary production (e.g., Lévy et al. 2018), in the restratification of surface layers (e.g., Boccaletti et al. 2007; Fox-Kemper et al. 2008), and in the vertical exchange between the surface and deep ocean (e.g., Balwada et al. 2018; Freilich and Mahadevan 2021; Su et al. 2018). To date, these submesoscale flows and their impacts have not been characterized globally. Even if presently available satellite altimetry data are pushed to their limit (e.g., Lawrence and Callies 2022), their resolution is ~100 km, such that the submesoscales at $\lesssim 10$ km are drowned in noise. The Surface Water and Ocean Topography (SWOT) mission, launched in late 2022, is expected to lower the noise floor by a factor of 50 compared to nadir altimeters (Desai 2018; Morrow et al. 2019), giving access to finer scales. The sea surface height (SSH) field at these finer scales, however, is expected to be a jigsaw puzzle of features due to geostrophically balanced turbulence and internal gravity waves. One will have to distinguish between signals arising from these drastically different types of motion in order to correctly interpret the new data.

Clear expectations for the variance of these signals will help with this distinction. We here develop such expectations for the power spectrum of SSH, widely used as a low-order statistical descriptor of this variance and its space–time scales. We focus on the balanced part of the signal because it is primarily this part of the flow that transport tracers. In addition, we are motivated to develop a prior estimate of the spectral content of the SSH field because such an estimate is needed for the objective mapping of altimetry data acquired with a complicated space–time sampling pattern (e.g., Wunsch 2006).

We currently have expectations for the balanced submesoscale SSH variance spectrum from theory and models—but few observations. Most observational constraints are conversions of near-surface kinetic energy (KE) spectra $\mathcal{K}(k)$ to SSH variance spectra, $\mathcal{S}(k) = (f/gk)^2\mathcal{K}(k)$, using geostrophic balance, where k is a horizontal wavenumber, f the local inertial frequency, and g the gravitational acceleration. Balanced submesoscale motion is strongly turbulent, and its KE spectrum often follows a power law $\mathcal{K}(k) \propto k^{-\alpha}$ (e.g., Callies and Ferrari 2013). The slope α depends on the presence or absence of submesoscale instabilities and is thought to be shaped by the turbulent dynamics induced by a combination of these instabilities and the mesoscale eddy field (Callies et al. 2016). The slope tends to vary between $\alpha \approx 2$ in winter and $\alpha \approx 3$ in summer (Callies et al. 2015; Lawrence and Callies 2022). According to geostrophic balance, these KE spectra give rise to SSH spectral slopes $\alpha + 2$ that vary between about 4 and 5, indicating that the SSH field associated with submesoscale turbulence is expected to be very smooth. Callies and Wu (2019)

Corresponding author: Charly de Marez, cdemarez@caltech.edu

DOI: 10.1175/JPO-D-22-0188.1

used these expectations to extrapolate the mesoscale energy captured by nadir altimeters down into the submesoscale range to estimate SWOT's expected resolution for balanced turbulence, finding a median of 51 or 74 km, depending on whether a slope of $\alpha + 2 = 4$ or 5 was used.

Analysis of nadir altimetry has yielded estimates of a spectral drop-off that in many regions is less steep than expected from these arguments (Fu and Ferrari 2008; Xu and Fu 2011, 2012; Vergara et al. 2019; Chen and Qiu 2021). It should be kept in mind, however, that the available scale range is small and that internal tides can contribute to the signal (Lawrence and Callies 2022). We here corroborate the expectation of steep SSH variance spectra for balanced flow using observations of SSH itself, and we extend this expectation by simultaneously constraining the time scales at which submesoscale SSH features evolve.

Recently, Villas Bôas et al. (2022) presented broadband SSH variance spectra off the coast of California, derived from aircraft lidar measurements and extending from wavelengths of ~100 km all the way down to ~1 m. If combined with satellite altimetry data, these spectra seem to confirm a steep drop-off of balanced signals. Unlike for KE spectra (Bühler et al. 2014), however, it is difficult to discern what part of the spectrum at scales $\gtrsim 1$ km is dominated by balanced motion versus internal waves, the same challenge that will be faced with SWOT data. We here use time-resolved data that can easily be separated into subinertial balanced and superinertial wave motion.

We present two methods to constrain the spectrum of SSH variance of balanced motion, using a pair of GPS buoys and a combination of moored current meters and altimetry. The GPS buoys are ~10 km apart, so they capture time-resolved submesoscale variations in SSH (cf. Callies et al. 2020). We use this information to constrain a model of the wavenumber–frequency content of balanced SSH variance (section 3), revealing that the spectral density must fall off steeply in wavenumber, as anticipated above. We also discover that the wavenumber–frequency spectrum is not separable, which enables another, more widely applicable method to constrain the wavenumber–frequency content of SSH. The nonseparability implies that frequency spectra of SSH variance and KE have different spectral slopes and that this difference constrains the wavenumber content of the balanced flow. We estimate this wavenumber content from a combination of nadir altimetry and moored current meters (section 4). We again find that the observations are consistent with SSH variance spectra that drop off steeply in wavenumber space. We discuss implications of these results for the SWOT mission and offer some comments on the global frequency content of balanced flow (section 5).

2. Data and processing

a. Altimetric along-track data

We use the along-track SSALTO/DUACS Delayed-Time Level-3 SSH measurements made by the *Jason-3* altimeter (Le Traon et al. 2017; distributed by AVISO+ with support from CNES; https://www.aviso.altimetry.fr) to estimate frequency spectra of SSH variance across the global ocean. The dataset consists of SSH time series along 254 tracks with ~7 km along-track spacing. The time series are 4 years long (2016–19) and have a spacing of 9.92 days. Frequency spectra are computed as follows. A Hann window is applied to each time series, and a discrete Fourier transform is taken of the product, giving a periodogram $|\hat{h}(\omega, x)|^2$ at each location x between 60°S and 60°N that is sampled by the satellite. The resulting 429 087 periodograms are then averaged over 2.5° × 2.5° boxes to yield the spectral estimate $\langle|\hat{h}(\omega, x)|^2\rangle$.

Significant tidal peaks are seen in the spectra even though a model for the external tide has been subtracted out from the along-track data. These remaining tidal signals may be due to errors in the model for the external tide or due to internal tides. In either case, these signals do not reflect the balanced motion of primary interest here and must be removed. Because the periods of the important tidal constituents are much shorter than the sampling period, tidal signals appear in the data as aliased signals at much longer periods, e.g., at an alias of 62 days for the semidiurnal constituent M_2 (Jacobs et al. 1992; Schlax and Chelton 1994a,b). In the fits described below, we therefore exclude the alias frequencies of the first 30 major constituents (by NOAA order) for each box. The annual (Sa) and semiannual (Ssa) peaks due to seasonal thermal expansion (Gill and Niiler 1973) also produce major peaks in the spectra and are similarly excluded. We see substantial variance in the M_2 alias peak in regions where the M_2 internal tide has previously been identified as important, for example off western Europe (e.g., Zhao et al. 2016). Our procedure, however, also excludes a substantial amount of variance in regions where internal tides have not been previously identified as significant, for example in western boundary regions. Our procedure might pick up the nontidal component of the spectrum at the frequency of tidal alias, or it might capture internal tides that have experienced frequency shifts large enough to evade the usually employed harmonic fits. Either way, given the high-frequency resolution of the spectral estimates and the broadband nature of the balanced flow, this potentially overzealous exclusion of a few frequencies does not affect the following analysis.

Once the tidal and seasonal signals are excluded, we fit our spectral estimates with the model spectrum (8), described below, using nonlinear least squares, yielding estimates of A_ω, ω_0, and s_ω for each 2.5° × 2.5° box across the global ocean (Fig. 1). The parameters are reasonably well constrained, with global median relative standard errors, estimated from the diagonal of the parameter covariance matrix and excluding the equatorial band, of 35%, 39%, and 12% for A_ω, ω_0, and s_ω, respectively.

It is worth noting that the noise-to-signal ratio of these frequency spectra is on average lower than 1% in the frequency range captured by the satellite-derived time series, indicating that measurement noise does not significantly affect the frequency spectrum of SSH variance, in contrast to corresponding wavenumber spectra (e.g., Xu and Fu 2012; Lawrence and Callies 2022). This noise-to-signal ratio is here obtained by first computing along-track wavenumber–frequency spectra; second defining a wavenumber k_{noise}, above which the

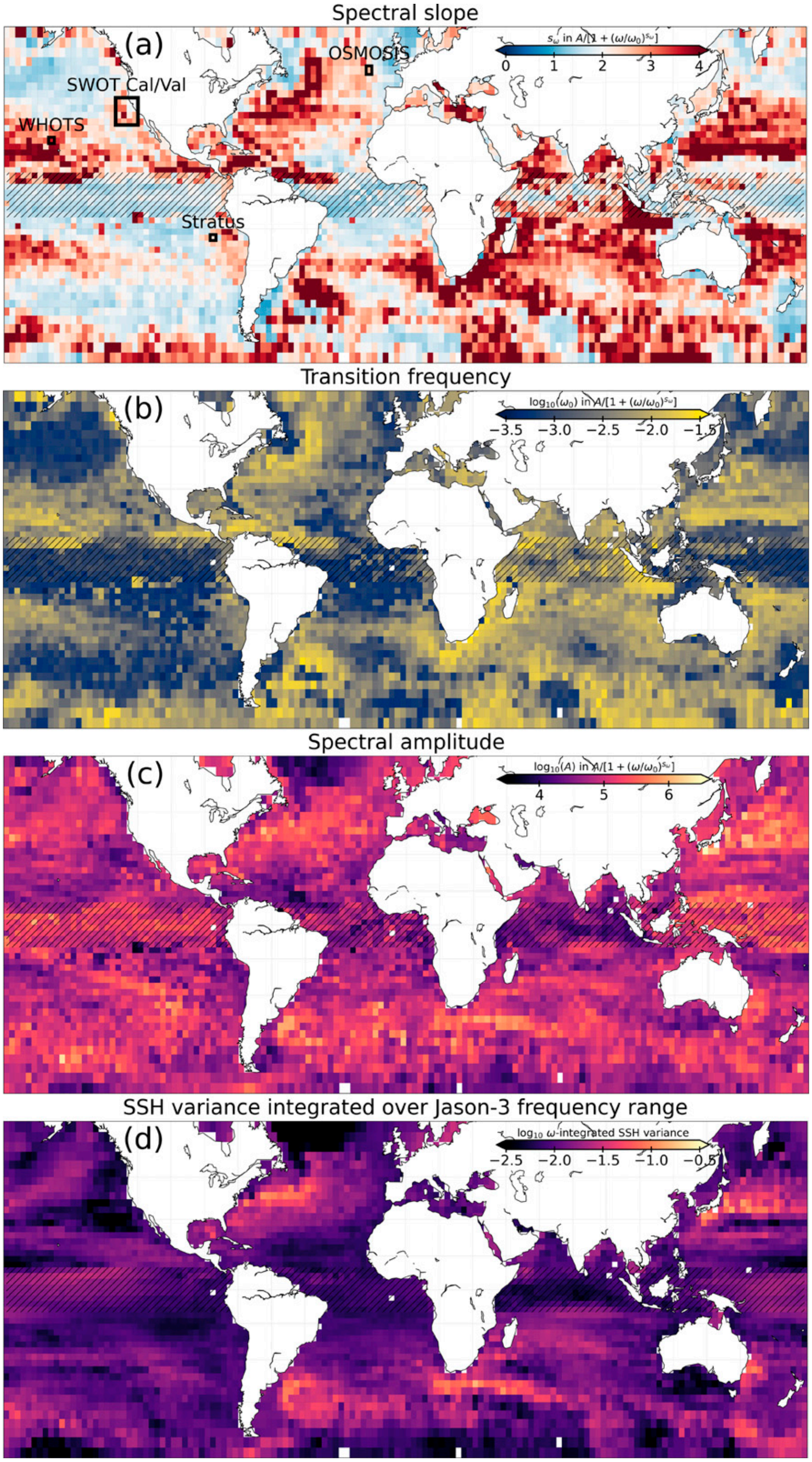

FIG. 1. Near-global estimates of the parameters of the model spectrum (8) from *Jason-3* time series. (a) Spectral slope s_ω and locations of in situ observations. (b) Transition frequency $\omega_0/2\pi$ (cpd). (c) Spectral amplitude A_ω (m^2 cpd^{-1}). (d) SSH variance integrated over the frequency range sampled by *Jason-3* (m^2). The equatorial region is hatched because distinct dynamics dominate the SSH signal there.

wavenumber marginal spectrum has a plateau due to the noise floor; third computing separate marginal frequency spectra for the signal and noise by integrating the wavenumber–frequency spectrum over the range $k < k_{\mathrm{noise}}$ for the signal and $k > k_{\mathrm{noise}}$ for the noise; and fourth computing the ratio between these two spectra. This procedure is performed in each 2.5° × 2.5° box, and the result is averaged over the global ocean.

Additionally, we use *Sentinel-3A* measurements to estimate a wavenumber spectrum at the site of the GPS buoys. We considered (i) six occupations of the track passing through the GPS buoys, collected every 27 days between 16 September 2019 and 29 January 2020, and (ii) all occupations between September and January during the 2016–22 period. We use 1400-km-long segments centered on the location of the buoys and estimate wavenumber spectra again applying a Hann window and averaging over the six occupations.

b. GPS buoy measurements

To study the spectral characteristics of SSH at higher frequencies and shorter scales than possible with satellite data, we take advantage of a set of moorings that were deployed as part of the 2019/20 SWOT prelaunch field campaign (Wang et al. 2022). These moorings were located 300 km west of Monterey Bay, California (see location in Fig. 1a). Data were collected over a 4-month period between September 2019 and January 2020. In addition to hydrographic measurements along the mooring lines, the northern and central moorings had a GPS buoy each at their top.

Advances in GPS technology—notably the emergence of compact, low-power geodetic-grade receivers and the development of advanced techniques for positioning remote platforms (Bertiger et al. 2010; Fund et al. 2013)—have conspired to enable accurate, long-term estimates of SSH in remote ocean locations (Haines et al. 2017; Penna et al. 2018). In cases where two or more GPS buoys are located in close proximity (order 10 km or less), precision of 1 cm or better has been demonstrated for the variability of the differential SSH, thanks in large measure to cancellation of common-mode GPS errors over short distances (Haines et al. 2019; Zhou et al. 2020). An overview of the GPS systems used in the SWOT prelaunch campaign, and the accompanying SSH estimates, is provided by Wang et al. (2022). Additional details of the measurements as they pertain to the current study are given in the appendix.

The dataset comprises 4-month-long time series with a 1-Hz sampling frequency. The inverse-barometer effect is removed using ERA-5 reanalysis data to yield an estimate of the SSH variations that produce pressure variations at a fixed reference level. In addition to this and further corrections detailed in the appendix, the M_2, S_2, K_1, O_1, N_2, P_1, Q_1, K_2, L_2, υ_2, M_1, J_1, OO_1, and $2N_2$ components of the tide are isolated in each time series using a nonlinear least squares fit of the corresponding tidal harmonic. During the measurement period, the sea state, characterized by the significant wave height (SWH), reached as high as 9 m. Since the SSH measurement becomes less reliable in high seas (Wang et al. 2022), we removed the parts of the time series with SWH exceeding 4 m. Reducing the threshold would not alter the conclusions but would increase the uncertainty due to more and longer data gaps. We applied a common mask to the two time series, defined by the times when one of the two SWH measurements exceeds the SWH threshold (note that individual masks represent 90% of the common mask). We compare different choices of the SWH threshold as well as the case without removing big sea states in the appendix.

We estimate the frequency spectrum of SSH variance $\langle|\hat{h}(\omega, x)|^2\rangle$ for each GPS buoy using the following procedure. First, tides are removed as described above. Second, the time series are divided into three chunks that overlap by 50%. Third, a 1-h boxcar moving average is applied to the time series to remove the signal due to surface gravity waves. Fourth, the time series are linearly interpolated across gaps on a 1-Hz grid. Fifth, a Hann window and a discrete Fourier transform are applied to each chunk, and the resulting periodograms are averaged for each buoy. Sixth, spectra are averaged into 10 logarithmically spaced frequency bins per decade. The same spectral estimation is performed for the time series of SSH differences between the two buoys (with the same SWH mask as before). To make sure this methodology yields robust spectral estimates, we ran it on synthetic data with known statistics (see the appendix). This indicates that the above procedure indeed recovers the theoretical spectrum of the prescribed statistics for frequencies $\omega/2\pi < 2 \times 10^1$ cpd (Fig. A1). The fall-off of the spectral estimate at frequencies $\omega/2\pi > 2 \times 10^1$ cpd is an artifact of the processing (mainly the moving average), so we exclude this frequency range from any further discussion.

Wang et al. (2022) found that the GPS-derived SSH time series had substantially more variance than one derived from steric height at periods between 1 and 10 days, attributed to sizable errors in the GPS data during high sea states. We overcome this problem by excluding the data during high sea states from the analysis (4-m SWH threshold).[1] To show the consistency during modest sea states explicitly, we compare the GPS-derived spectrum to the equivalent spectrum estimated from the bottom pressure and full-depth hydrographic measurements available at the northern mooring (cf. Wang et al. 2022). Vertically integrating hydrostatic balance suggests that the pressure at $z = 0$, the dynamical quantity of interest, can be obtained in two ways (e.g., Gill and Niiler 1973):

$$\frac{p(0)}{\rho_0 g} = \frac{p(-H)}{\rho_0 g} + \frac{1}{g}\int_{-H}^{0} b\,dz = h + \frac{p_{\mathrm{atm}}}{\rho_0 g}, \tag{1}$$

where p is the pressure anomaly, ρ_0 is a reference density, H is the bottom depth, b is the buoyancy anomaly, h is the SSH anomaly relative its mean position at $z = 0$, and p_{atm} is the atmospheric pressure anomaly. All anomalies are relative to a time mean. The first expression in (1) can be evaluated with

---

[1] These errors are most likely caused by uncorrected Lagrangian mean offsets in the heights obtained from the GPS buoys. We hope to ascertain this preliminary explanation in future work.

the bottom pressure as measured by a bottom pressure recorder and the steric height as estimated from hydrographic measurements between 2000-m depth and the surface. The second expression in (1) is what we call the GPS-derived SSH: the height h as measured directly by the GPS buoy, corrected for the inverse-barometer effect (final term). We compute the frequency spectrum from the bottom pressure and steric height measurements using the same procedure as above. The two spectral estimates agree to within the uncertainty, indicating that the above equation is closed to an acceptable level (Figs. 2a and A1). The consistency of the two entirely independent data sources increases our confidence in the GPS data, which we use as a backbone of the analysis in section 3.

c. *Moored current meter data and processing*

We use near-surface current measurements from three different mooring locations (see Fig. 1a) to compute the frequency spectrum of surface KE. The datasets are the following: the Ocean Surface Mixing, Ocean Submesoscale Interaction Study (OSMOSIS) mooring array, located at about 48.7°N, 16.2°W, which provides yearlong time series (September 2012–13, centered on March, i.e., winter/spring) with a 10-min sampling period obtained from nine current meters (acoustic current meters, ACMs) located at ~50-m depth and separated by a maximum horizontal distance of about 20 km (Buckingham et al. 2016); the WHOI Hawaii Ocean Time Series Site (WHOTS), located at about 22°N, 158°W, which provides 10 yearlong time series (spanning 2004–14, on average centered on December/January, i.e., winter) obtained from vector measuring current meters (VMCMs) or ACMs (depending on the year), at ~10-m depth, with a 1-min sampling period (Kamphaus 2014); the Stratus Project mooring located at about 22°S, 85°W, which provides 13 yearlong time series (spanning 2000–14, on average centered on April/May, i.e., fall) obtained from VMCMs or ACMs (depending on the year), at ~10-m depth, with a ~10-min average sampling period (Weller 2015). For each mooring and each year, we compute the KE frequency spectrum using the windowed zonal and meridional velocity time series as described for SSH above. We then average over the years for each mooring and over the nine moorings for the OSMOSIS array.

We interpret the subinertial currents as geostrophically balanced because geostrophic currents typically dominate over wind-forced Ekman currents at periods longer than 10 days (Elipot and Gille 2009) and because the current meters are at least 10 m below the surface, where Ekman currents have decayed to some degree. Elipot and Gille (2009) estimated leading-order ageostrophic surface currents at periods between 1 and 10 days but calculated the ageostrophic component by subtracting altimetric estimates from drifter observations, with the altimetric estimates relying on objective mapping that is expected to reduce the power at periods shorter than 10 days. As a result, and as acknowledged by the authors, their estimate for the ageostrophic component at these short periods is likely spuriously high.

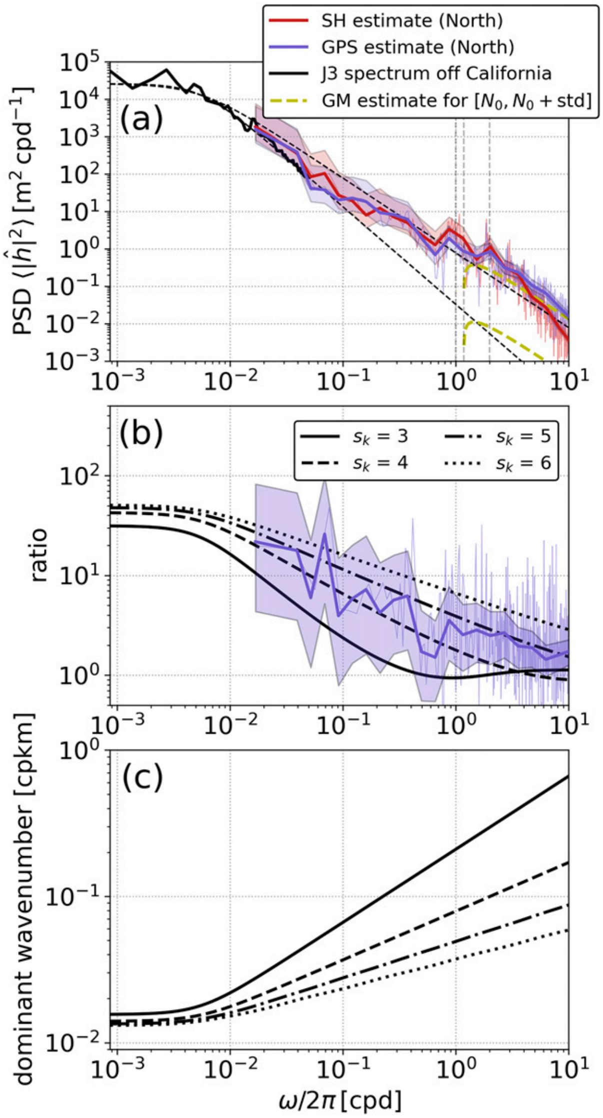

FIG. 2. Constraint on submesoscale SSH variance from a pair of GPS buoys. (a) Frequency spectra of SSH variance at the northern mooring from the GPS buoy (blue), bottom pressure plus steric height (red), and *Jason-3* (black solid). Also shown are the model spectra with $s_\omega = 2.0$ and 2.6 (black dashed), Garrett–Munk spectra (green dashed), and the frequencies of the diurnal tide, semidiurnal tide, and inertial motion (vertical dashed). (b) Ratio spectrum from the model spectrum with $s_\omega = 2.0$ and various values of s_k (black) and observations (blue). (c) Dominant wavenumber k_d for $s_\omega = 2.0$ and the same values of s_k as in (b). Envelopes around spectral estimates show 95% confidence intervals.

d. *Spectral estimation error*

Confidence intervals on spectral estimates are computed using standard protocol (e.g., Thomson and Emery 2014). We calculate 95% confidence intervals for all spectral estimates using a χ^2 distribution, assuming the underlying statistics are Gaussian. The number of degrees of freedom are taken to be twice the number of time chunks or track occupations. For the frequency spectra derived from in situ data, we have three chunks and therefore six degrees of freedom. We assume that the Hann-windowed time chunks are independent despite the 50% overlap, which produces only a slight overestimate of the degrees of freedom (Percival and Walden 1993). We further accumulate degrees of freedom when frequency-bin averaging (e.g., Fig. 2b). For the *Sentinel-3A* data, we have 12 degrees of freedom when using the 2021 data only and 72 degrees of freedom when using the full record.

For an estimate $\hat{G}(\omega)$ of a spectrum $G(\omega)$, the following inequality holds with a probability $1 - \alpha$:

$$\frac{\nu \hat{G}(\omega)}{\chi^2_{1-\alpha/2,\nu}} < G(\omega) < \frac{\nu \hat{G}(\omega)}{\chi^2_{\alpha/2,\nu}}, \tag{2}$$

where ν is the number of degrees of freedom, χ^2 denotes the cumulative distribution function, and $\alpha = 0.05$ for a 95% confidence level. For an estimate $\hat{H}(\omega)$ of the ratio spectrum $H(\omega)$, the same argument applies, except that the estimate is now $\mathcal{F}$ distributed, and the corresponding inequality is

$$\frac{\hat{H}(\omega)}{\mathcal{F}_{1-\alpha/2,\nu,\nu}} < H(\omega) < \frac{\hat{H}(\omega)}{\mathcal{F}_{\alpha/2,\nu,\nu}} \tag{3}$$

where $\mathcal{F}$ is the cumulative distribution function of an $\mathcal{F}$-distributed random variable.

3. Constraints from a pair of GPS buoys

Here, we make use of the idea that spatially separated mooring observations provide constraints on the wavenumber–frequency content of the observed signal (e.g., Garrett and Munk 1972; Callies et al. 2020). We use a pair of GPS buoys to constrain the wavenumber–frequency spectrum of SSH variance. Given that a single pair of buoys cannot constrain the full wavenumber–frequency content, we assume a model spectrum that is consistent with available observations and constrain its parameters. We use the model spectrum

$$\mathcal{S}(k, \omega) = \frac{A}{[1 + (k/k_0)^a + (\omega/\omega_0)^b]^c}, \tag{4}$$

where A sets the overall amplitude of the spectrum; k_0 and ω_0 set the wavenumber and frequency at which the spectrum transitions from a plateau at low frequencies and wavenumbers to a power-law drop-off; and a, b, and c control both the shape of this transition and the behavior at high wavenumbers and frequencies. Here, k is an along-track wavenumber, not the magnitude of a two-dimensional wavenumber vector. The model spectrum (4) is similar to the one proposed by Wortham and Wunsch (2014)—with two key differences. First, focusing on smaller scales here, we exclude the exponential part of their model spectrum that captured the dominance of westward propagation. Second, we give the power-law part of the model spectrum a nonseparable form. We will see below that this nonseparability is required by the data. The form (4) is a simple nonseparable model that has the requisite power-law behavior at high frequencies and wavenumbers and a plateau at low frequencies and wavenumbers.

From a GPS buoy, we can estimate the marginal frequency spectrum

$$\mathcal{S}_\omega(\omega) = \int_{-\infty}^{\infty} \mathcal{S}(k, \omega)\, dk = \frac{A_\omega}{[1 + (\omega/\omega_0)^b]^{c-1/a}}, \tag{5}$$

where A_ω depends on a, b, c, and k_0 but not on ω. The spectral slope s_ω in the high-frequency limit is therefore $s_\omega = b(c - 1/a)$. Similarly, the marginal wavenumber spectrum is

$$\mathcal{S}_k(k) = \int_0^{\infty} \mathcal{S}(k, \omega)\, d\omega = \frac{A_k}{[1 + (k/k_0)^a]^{c-1/b}}, \tag{6}$$

where A_k is independent of k. We would like to constrain the spectral slope s_k in the high-wavenumber limit $s_k = a(c - 1/b)$, i.e., the drop-off of SSH variance at submesoscales. It follows that

$$a = \frac{s_k s_\omega - 1}{c(s_\omega - 1)} \quad \text{and} \quad b = \frac{s_k s_\omega - 1}{c(s_k - 1)}. \tag{7}$$

For a given s_k and s_ω, the parameter c merely controls the behavior near the transition between the plateau and power-law range. This transition is poorly constrained by the data. We set $s_\omega = b$—or, equivalently, $c = 1/a$—and fit the marginal spectrum in the form

$$\mathcal{S}_\omega(\omega) = \frac{A_\omega}{1 + (\omega/\omega_0)^{s_\omega}}. \tag{8}$$

With this choice, all parameters can be determined using (7) for a given set of s_ω and s_k.

The spectral slope s_ω can be estimated from the observed SSH time series. We can then compare predictions based on various assumptions for s_k to the observations of the variance spectrum of the SSH difference between the two moorings. The ratio of the SSH variance spectrum to half the variance spectrum of this difference can be predicted to be (cf. Babiano et al. 1985)

$$\frac{\mathcal{S}_\omega(\omega)}{\mathcal{D}_\omega(\omega)} = \frac{\int_{-\infty}^{\infty} \mathcal{S}(k, \omega)\, dk}{\int_{-\infty}^{\infty} \mathcal{S}(k, \omega)(1 - \cos kr)\, dk}, \tag{9}$$

which is most easily evaluated numerically for the mooring distance $r = 13$ km. This calculation assumes spatial homogeneity in the statistics, which is consistent with the data: the SSH variance spectra at the two buoys are indistinguishable (cf. Wang et al. 2022, Fig. 14). Note that if the wavenumber–frequency spectrum was separable, i.e., if we could write $\mathcal{S}(k, \omega) = \Omega(\omega)\Lambda(k)$ with Ω describing the frequency dependence and Λ describing the wavenumber dependence, the frequency dependence would cancel in (9), and the ratio spectrum would be a constant in ω.

To estimate s_ω and ω_0, we combine the GPS buoy data with nearby *Jason-3* data. The frequency spectra obtained from these two sources match in the overlapping frequency range 3×10^{-2} cpd $< \omega/2\pi < 6 \times 10^{-2}$ cpd (Fig. 2a). This combination

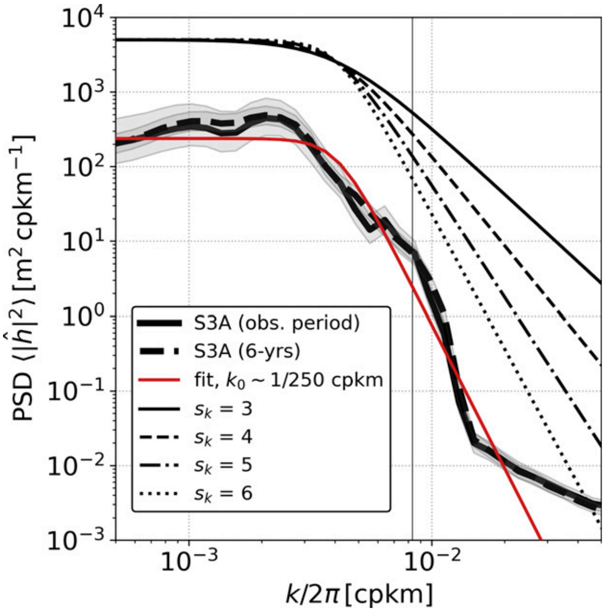

FIG. 3. Wavenumber spectrum of SSH variance along a *Sentinel-3A* track passing through the mooring locations (Fig. 5). Shown are the spectral estimates from six satellite occupations during the in situ experiment (solid line) and from the full record (dashed line), together with a fit of the model spectrum (6) that gives $s_k = 5.5 \pm 0.5$ and $k_0/2\pi = (4 \pm 2) \times 10^{-4}$ cpkm (red). Also shown is the model spectrum (6) for other values of s_k (thin black). The envelope of the spectral estimate indicates a 95% confidence interval. The vertical thin black line marks the wavenumber (120 km)$^{-1}$.

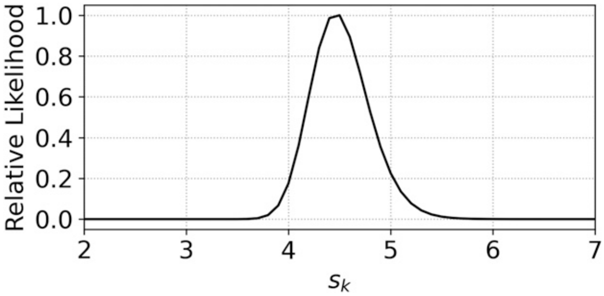

FIG. 4. Relative likelihood for the different wavenumber spectral slopes s_k given the observed ratio shown in Fig. 2b.

yields a transition frequency $\omega_0/2\pi = 5.5 \times 10^{-3}$ cpd and a high-frequency spectral slope around $s_\omega = 2.0$ in the subinertial range, substantially less than the $s_\omega = 2.6$ estimated from the *Jason-3* data only (Fig. 2a). This somewhat large difference is likely the result of the limited time window in which GPS data are available (4 months) compared to the long *Jason-3* time series (4 years). Nevertheless, the estimated slopes fall into the range expected from previous observations and numerical simulations (Stammer 1997; Arbic et al. 2012). We use $s_\omega = 2.0$ in the analysis that follows because this characterizes the spectrum during the time of observation (using $s_\omega = 2.6$ would not change our conclusions). Finally, to predict the ratio $\mathcal{S}_\omega(\omega)/\mathcal{D}_\omega(\omega)$ for various s_k, we require an estimate for k_0. The transition from a low-wavenumber plateau to a power law occurs at mesoscales, so we can estimate it from *Sentinel-3A* data, whose ground track passes through the mooring site. A fit of the *Sentinel-3A*–derived wavenumber spectrum yields $k_0/2\pi = (250\ \text{km})^{-1}$ (Fig. 3), which agrees with estimates from Lawrence and Callies (2022).

We are now in a position to predict $\mathcal{S}_\omega(\omega)/\mathcal{D}_\omega(\omega)$ using the model spectrum and compare this prediction to the observed ratio. First, we note that the ratio estimated from observations is decreasing with frequency (Fig. 2b), indicating that the underlying wavenumber–frequency spectrum of balanced flow is not separable. The ratio drops from ~20 at $\omega/2\pi = 2 \times 10^{-2}$ cpd to ~2 at $\omega/2\pi = 1$ cpd. We disregard higher frequencies because the model spectrum is meant to capture balanced motion only, and the high frequencies may contain signals from tides and inertia–gravity waves. Second, we predict $\mathcal{S}_\omega(\omega)/\mathcal{D}_\omega(\omega)$ for $s_k = 3$, 4, 5, and 6, and we evaluate the consistency of these predictions with the data. While the error bar is sizable, slopes between $s_k = 4$ and 5 are most consistent with the data (Fig. 2b). The relative likelihood, computed assuming the spectral estimates are *F*-distributed around the theoretical values and independent at different frequencies, has a well-defined peak between $s_k = 4$ and 5 (Fig. 4). The data therefore support our expectation that SSH variance spectra fall off steeply with wavenumber k.

This conclusion is consistent with the drop-off seen in available altimetry data. We use data from *Sentinel-3A*, whose ground track passed through the mooring site, from six passes during the mooring deployment (Fig. 5). While only a narrow wavenumber range below the mesoscale plateau is captured before noise takes over, a steep drop-off with $s_k \geq 4$ is seen (Fig. 3). There is a bump in the *Sentinel-3A* spectrum at about $k/2\pi = 8 \times 10^{-3}$ cpkm. It is also seen in the wavenumber spectrum computed from all *Sentinel-3A* occupations between September and January during the period of 2016–22, i.e., averaged over 6 years. It is therefore likely the signature of the first-mode internal M_2 tide (with wavelength 120 km, see Ray and Zaron 2016).

The presence of submesoscale balanced motion can be discerned from a snapshot of sea surface temperature during the period of observations. Warm filaments and submesoscale vortices can be seen at the edge of a mesoscale eddy that is located to the east of the mooring location (Fig. 5). These submesoscale structures are likely the result of submesoscale instabilities induced by the strong potential vorticity gradients at the edge of the eddy (Callies et al. 2016; Brannigan et al. 2017; Ioannou et al. 2017; Taylor et al. 2018; de Marez et al. 2020). Our analysis shows that even such comparatively strong submesoscale features produce a weak SSH signal—the SSH variance spectrum still falls off with $s_k \geq 4$.

To confirm that the observations constrain submesoscale SSH features, we estimate the dominant wavenumber as a function of frequency from the model spectrum (4) as

$$k_d = \frac{\int_{-\infty}^{\infty} k\mathcal{S}(k,\omega)\,dk}{\int_{-\infty}^{\infty} \mathcal{S}(k,\omega)\,dk}, \tag{10}$$

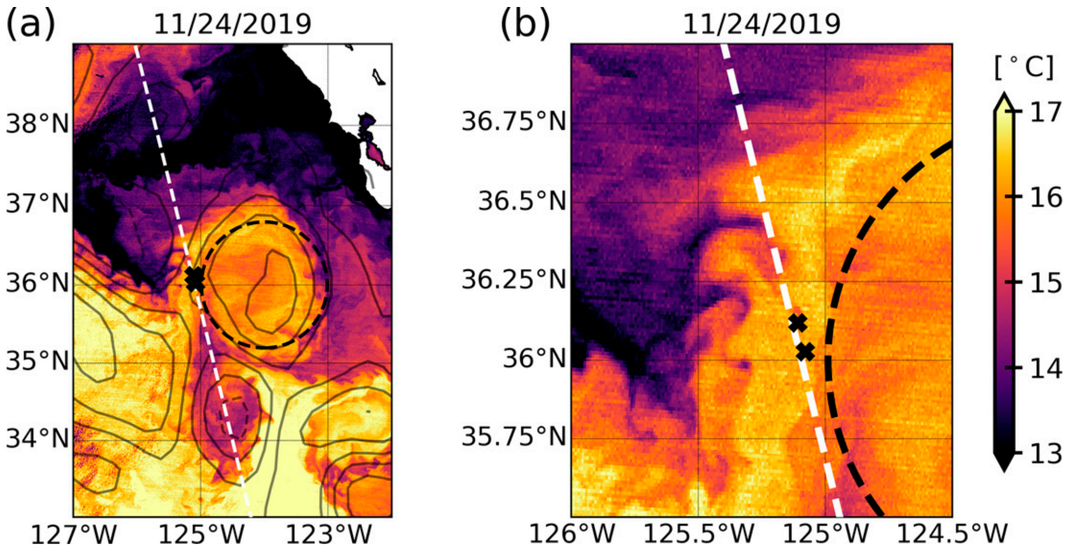

FIG. 5. Presence of submesoscale features during the SWOT prelaunch campaign. (a) Snapshot of SST (from VIIRS *Suomi-NPP* L2 data) off the coast of California (shading) and SSH field (from DUACS L4 NRT data) (contours; 5-cm interval). (b) Zoom-in of the SST field. Also shown in both panels are the locations of the two GPS buoys (black crosses), the *Sentinel-3A* ground track (white dashed line), and a reference circle with radius 110 km (black dashed line).

using the same parameters as above and several values of s_k. For any plausible set of parameters ($3 < s_k < 6$, and $1 < s_\omega < 3$), the dominant wavenumber increases with ω, showing that small scales dominate at high frequencies. For instance, for $s_\omega = 2.0$ and $s_k = 4$, the dominant wavelength at a period of 1 day is about 10 km (Fig. 2c).

We restricted our analysis to subinertial frequencies to focus on the balanced flow, but the GPS buoys also shed light on superinertial processes. Tidal and superinertial frequencies are clearly distinct from the low-frequency behavior (Fig. 2a). Away from the tidal peaks, the high-frequency signal may be dominated by internal waves. We compute the Garrett–Munk (GM) estimate for SSH variance following Callies and Wu (2019). We use an average buoyancy frequency $N_0 = 3 \times 10^{-3}\ \mathrm{s}^{-1}$, estimated using Argo float 4903011, which sampled the water column near the buoy locations during the 4-month sampling period. We show the resulting GM spectrum, both for N_0 and N_0 plus one standard deviation seen in the Argo data (Fig. 2a), because the buoys were located at the edge of an anticyclonic eddy (Fig. 5), where the stratification is likely enhanced. The GM spectrum has a -2 slope and an amplitude comparable to the spectrum estimated from the GPS buoys. It is therefore plausible that the superinertial signal in the observed frequency spectrum is dominated by internal waves. These waves are expected to dominate over balanced motion at small scales because they decay much less rapidly with wavenumber (Callies and Wu 2019).

4. Constraints from a combination of moored current meters and altimetry

The conclusion that the SSH variance spectrum is not separable in its dependence on wavenumber and frequency suggests another approach to constrain the wavenumber drop-off s_k from available observations. The nonseparability implies that frequency spectra of SSH variance and KE have different spectral slopes. For the model spectrum (4), the frequency spectrum of SSH has a slope $s_\omega = b(c - 1/a)$, as discussed above, whereas the frequency spectrum of the KE in the cross-track velocity component is (after applying the geostrophic relation)

$$\mathcal{K}_\omega(\omega) = \frac{g^2}{f^2}\int_{-\infty}^{\infty} k^2 \mathcal{S}(k, \omega)dk = \frac{A'_\omega}{[1 + (\omega/\omega_0)^b]^{c-3/a}}, \qquad (11)$$

where A'_ω is independent of ω. The slope of the KE frequency spectrum in the high-frequency limit is therefore $s'_\omega = b(c - 3/a)$. Following the choice for c described in the previous section, this leads to the marginal frequency spectrum of KE to take the form

$$\mathcal{K}_\omega(\omega) = \frac{A'_\omega}{[1 + (\omega/\omega_0)^b]^{s'_\omega/b}}, \qquad (12)$$

which is then used for the fitting. Together with $s_k = a(c - 1/b)$, this allows us to determine the wavenumber drop-off from frequency information only:

$$s_k = \frac{3s_\omega - s'_\omega - 2}{s_\omega - s'_\omega}. \qquad (13)$$

If the frequency slopes s_ω and s'_ω can be estimated from altimetry and moored current meters, and if the underlying wavenumber–frequency spectrum can be approximated with the model (4), then s_k can be estimated.

We compute the near-surface frequency spectra of KE at three distinct mooring locations. Using nonlinear least squares, we simultaneously fit the resulting KE spectrum with the

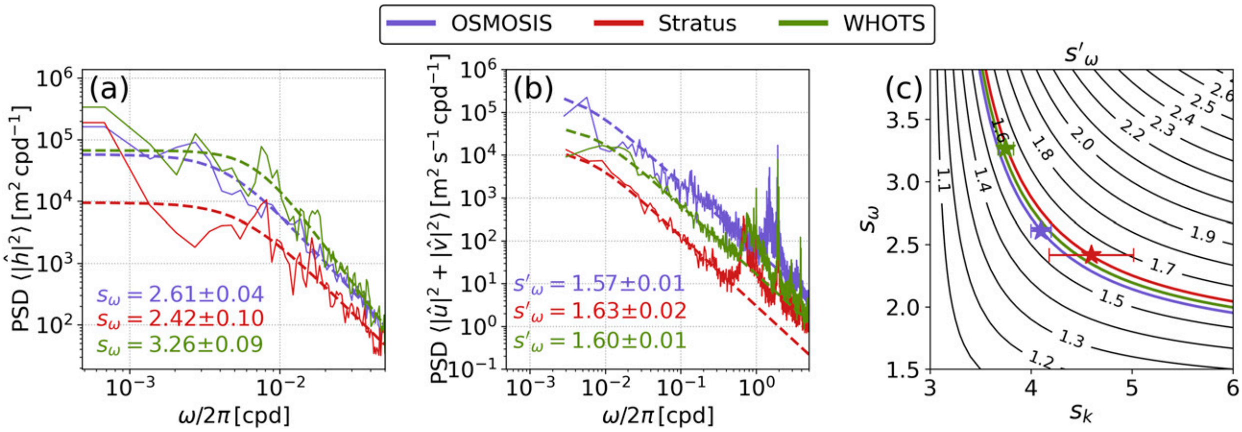

FIG. 6. Constraints on submesoscale SSH variance from moored current meters and satellite altimetry. (a) Frequency spectra of SSH variance from *Jason-3* along-track data in the boxes over the mooring locations (solid lines; see Fig. 1a for locations), together with fits of the model spectrum (8) (dashed lines) and the resulting spectral slope s_ω (in the corresponding color). (b) Frequency spectra of KE from moored near-surface current meters (solid lines), together with fits of the model spectrum (12) (dashed lines) and the spectral slope s'_ω (in the corresponding color). (c) Resulting constraint on the wavenumber spectral slopes s_k from (13). Contours show the slope of the KE spectrum in frequency space s'_ω as a function of the SSH wavenumber and frequency spectral slopes s_k and s_ω. The colored lines show the observed values of s'_ω for each mooring, and the stars mark the position of the observed s_ω values. The resulting values of s_k can be read off the horizontal axis, and the 2σ uncertainty is indicated by error bars.

model spectrum (12) and the corresponding SSH variance spectrum with the model spectrum (8), obtaining a shared value of ω_0 (Fig. 6b). We restrict the fit to subinertial frequencies, such that the estimated s'_ω represents balanced motion only. We compare these KE spectra to frequency spectra of SSH variance estimated from *Jason-3* data at the same locations (Fig. 6a). While *Jason-3*'s return period of about 10 days limits the frequency resolution, the slopes in the high-frequency limit can be estimated with reasonable confidence.

In all three locations, the frequency spectra of SSH variance exhibit slopes $s_\omega > 2$ (Fig. 6a). The KE spectra fall off following power laws remarkably closely at subinertial frequencies and exhibit slopes in the range $1.5 < s'_\omega < 2.0$ (Fig. 6b). The KE spectral slopes are more similar between the three locations than those for SSH variance. Taken together, these slopes in frequency space constrain the drop-off in wavenumber space, following (13), to be $s_k = 4.1 \pm 0.1$ for OSMOSIS, 4.6 ± 0.4 for Stratus, and 3.8 ± 0.1 for WHOTS. All uncertainties are given as one standard deviation, calculated from the slope errors using linearized Gaussian error propagation.

For all three locations, the wavenumber spectrum is again constrained to fall off steeply. The drop-off is steeper at Stratus than it is for the other two locations, indicating relatively weak submesoscales at Stratus (KE slope $\alpha = 2.6 \pm 0.4$) and strong submesoscales at OSMOSIS ($\alpha = 2.1 \pm 0.1$) and WHOTS ($\alpha = 1.8 \pm 0.1$). These differences may be the result of seasonal variations in the submesoscale energy level (cf. Callies et al. 2015, 2020). The time series from moored current meters are typically 1 year long, and the windowing emphasizes the season these 1-yr chunks are centered on. The OSMOSIS and WHOTS time series are typically centered on winter, when submesoscale turbulence is energetic, whereas the Stratus time series tend to be centered on fall, a season when the submesoscale activity is expected to be weak. The fact that the estimated submesoscale SSH variance aligns with expectations adds confidence that the model spectrum (4) can capture the structure of the wavenumber–frequency distribution of balanced SSH variance.

5. Discussion

a. *Implications for high-resolution altimetry*

The study of time series from a pair of GPS buoys (section 3) and from a combination of moored current meters and altimetry (section 4) provides two independent lines of evidence suggesting that the submesoscale SSH variance spectrum of balanced motion falls off steeply, $s_k \gtrsim 4$. This is consistent with KE wavenumber spectra obtained from shipboard ADCP that tend to fall off with spectral slopes between 2 and 3 (e.g., Callies and Ferrari 2013; Shcherbina et al. 2013; Callies et al. 2015; Rocha et al. 2016; Qiu et al. 2017; Chereskin et al. 2019; Sérazin et al. 2020; Soares et al. 2022), and it matches expectations from numerical simulations and theoretical arguments (Charney 1971; Klein et al. 2008; Capet et al. 2008; Sasaki et al. 2014; Callies et al. 2016; McWilliams 2016; Taylor and Thompson 2023). It strongly suggests that the more gentle drop-off inferred from nadir altimetry in many regions (e.g., Fu and Ferrari 2008; Xu and Fu 2011, 2012; Vergara et al. 2019; Chen and Qiu 2021) is caused by processes other than balanced motion. Internal tides and an imperfect removal of altimetry noise are primary suspects. Similarly, if SWOT reveals SSH variance that falls off less steeply ($s_k < 4$), the leading hypothesis should be that this is caused by superinertial motion rather than very energetic balanced turbulence.

As discussed in Callies and Wu (2019), the steep spectral drop-off for balanced motion makes it exceedingly difficult to observe ~10-km-scale submesoscale turbulence with satellite altimetry. Even when submesoscale turbulence is energetic, i.e., when $s_k = 4$, the 50-fold decrease in the noise level expected for SWOT compared to the Jason-class altimeters (Desai 2018) yields a resolution increased by a factor of merely $50^{1/4} = 2.7$. It also means that superinertial motion may quickly dominate the SSH signal at submesoscales—more strongly than in KE because the conversion between KE and SSH variance favors superinertial motion. It suggests that in the long term, submesoscale balanced motion may be more easily accessed with direct space-borne observations of velocities, as recently proposed (Rodríguez et al. 2019). The surface velocity field is simply not as smooth as the SSH field (cf. Chelton et al. 2019).

b. *Understanding the frequency content*

It should be emphasized that the model spectrum (4) is completely empirical. It is a convenient description of the wavenumber–frequency variability with a limited set of parameters. Its nonseparability propriety appears to be required by observations, but its shape has no theoretical underpinning.

The simplest model connecting the wavenumber and frequency domains is Taylor's hypothesis (Taylor 1938; Ferrari and Wunsch 2010; Arbic et al. 2012): the flow field is assumed to be effectively frozen as it is advected past a fixed observer with some constant velocity U. This concentrates the energy along a line $\omega = Uk$ in wavenumber–frequency space. Such a spectrum is not separable, consistent with our observations. But it also predicts that the wavenumber and frequency slopes should be equal, which is clearly not the case for the observed SSH field (Figs. 2a,b) and also does not hold up in idealized simulations of quasigeostrophic turbulence (Arbic et al. 2012).

A dimensional argument by Tennekes and Lumley (1972), devised for three-dimensional, homogeneous turbulence but potentially applicable more generally, predicts a universal $s'_\omega = 2$. Spectra from all three moored current meters analyzed here, however, exhibit a slope that is significantly different from this prediction (Fig. 6b). Furthermore, according to (13), $s'_\omega = 2$ and $4 < s_k < 5$ would constrain the slope of the SSH variance spectrum to fall into the range $4/3 < s_\omega < 3/2$. The observed range is much broader, and the slopes tend to be larger (Fig. 1a).

While the Taylor hypothesis fails, it is still likely that Doppler shifting shapes the frequency content at submesoscales. Callies et al. (2020) argued that the time scales registered by an Eulerian observer are substantially shorter than the time scales of Lagrangian evolution. The Doppler shifting will be more complicated than in Taylor's case if the dominant flow is a turbulent mesoscale eddy field. In this context, it is interesting to observe that the frequency roll-off in altimetric SSH variance spectra exhibits patterns similar to the mesoscale energy levels (Figs. 1a,d). Frequency spectra tend to fall off steeply where mesoscale eddies are strong and more gently where mesoscale eddies are weak. The transition frequency ω_0, characterizing the dominant time scale, has a similar pattern (Figs. 1c,d). More work is needed to turn these observations into a quantitative theory.

6. Conclusions

The observational data presented here constrain the SSH variance spectrum due to submesoscale balanced turbulence to fall off steeply with wavenumber, consistent with prior expectations. This is true even when the submesoscale turbulence is energetic and submesoscale instabilities can be identified in SST images. Two types of constraints were presented, both obtained from time-resolved observations, for which it is straightforward to isolate subinertial balanced motion. In all four locations studied, spanning the midlatitude and subtropical ocean, the observations are consistent with a wavenumber roll-off between $s_k = 4$ and 5. This substantiation of expectations based on shipboard measurements, numerical models, and theory suggests that previous estimates of spectral slopes from nadir altimetry may have been biased low because unbalanced motion has contributed signals at high wavenumbers or instrument noise has been removed imperfectly. This result will aid the interpretation of data from the SWOT mission, suggesting that submesoscale SSH variance that is observed to be in excess of this expectation is very likely due to unbalanced motion or instrument noise.

The characterization of meso- and submesoscale turbulence in the frequency domain, used here primarily as a tool to constrain the spatial structure, poses interesting theoretical questions. Large variations across the global ocean are observed in the frequency-domain roll-off of SSH variance spectra, far from a universal behavior. Slope variations tend to track the variations of mesoscale energy, suggesting Doppler shifting to play a role in shaping the frequency spectra. A quantitative explanation for this behavior would be a good target for future work.

In addition to the physical insight, this study also confirmed and went beyond the results shown in Wang et al. (2022). It demonstrated the accuracy of the open-ocean GPS-buoy SSH measurements during low sea state conditions and their utility in studies of submesoscale dynamics.

Acknowledgments. C.d.M. and J.C. were supported by NASA Grant 80NSSC20K1140. D.R. was supported by a Resnick Sustainability Institute WAVE Fellowship. J.W. and B.H. were supported by the SWOT project. A portion of this research was carried out at the Jet Propulsion Laboratory, California Institute of Technology, under a contract with the National Aeronautics and Space Administration.

Data availability statement. The atlas of SSH frequency spectrum properties and related scripts to compute it, as well as mooring time series are available at https://github.com/demarez/sshspectrum. NRT CMES GRIDDED data are available on the dedicated Copernicus repository (https://resources.marine.copernicus.eu/product-detail/SEALEVEL_GLO_PHY_CLIMATE_L4_MY_008_057/INFORMATION). Similarly, *Jason-3* and *Sentinel-3A* along-track data are available at https://resources.marine.copernicus.eu/product-detail/SEALEVEL_GLO_PHY_L3_MY_008_062/INFORMATION. VIIRS *Suomi-NPP* L2 data are available on NASA's Earthdata website (https://earthdata.nasa.gov/). OSMOSIS mooring data are available on BODC's repository (https://www.bodc.ac.uk/projects/data_management/uk/osmosis/data_delivery/). Stratus and WHOTS mooring data are available on WHOI's repository (https://uop.whoi.edu/currentprojects/). GPS buoy data are available on Jet Propulsion Laboratory's repository https://podaac.jpl.nasa.gov/dataset/SWOT_PRELAUNCH_L2_GPS_V1.

APPENDIX

Discussion on the GPS-Derived Frequency Spectra

Applying a SWH threshold of 4 m (resp. 3 m) on the GPS-derived time series introduces an average gap of 10 h (resp. 29 h), with a maximal gap of 41 h (resp. 124 h), altogether corresponding to 12% (resp. 37%) of the time series. Despite this, the GPS-derived SSH variance spectra for the two thresholds are very similar and consistent with the estimate derived from steric height (Fig. A1a). In contrast, applying no threshold increases the variance level between 1 and 10 days (in addition to the high frequencies), recovering the result of Wang et al. (2022). This shows that high sea states must be excluded because GPS errors increase and that the gaps introduced in the time series by this exclusion do not substantially affect the spectral estimation. Judged by the consistency with the steric-height-derived estimate, we deem a 4-m threshold optimal.

We further confirm that the interpolation and spectral analysis is robust by using synthetic data with known statistics. If $b = 2$, the frequency spectrum (8) can be rewritten as

$$\mathcal{S}_\omega(\omega) = \frac{A}{[1 + (\omega/\omega_0)^2]^{s/2}}, \qquad \text{(A1)}$$

which is the spectral density of a Matérn process and for $s = 2$ has the closed-form covariance function

$$C(\tau) = \frac{1}{2} A\omega_0 e^{-\omega_0|\tau|}, \qquad \text{(A2)}$$

where τ is the time lag. We generate synthetic data with this covariance by starting with a time vector $\mathbf{t}$ containing the sampling times of the GPS buoy, with different times removed based on a given SWH threshold. We then compute the covariance matrix $\mathbf{C}$ with elements $c_{ij} = C(t_i - t_j)$. The covariance matrix being positive definite, its Cholesky decomposition can be computed to give $\mathbf{C} = \mathbf{L}\mathbf{L}^\mathrm{T}$. We then apply $\mathbf{L}$ to a vector $\mathbf{x}$ of random numbers drawn from independent normal distributions with unit variance: $\mathbf{y} = \mathbf{L}\mathbf{x}$. Since $\mathbf{x}$ has the covariance matrix $\langle \mathbf{x}\mathbf{x}^\mathrm{T} \rangle = \mathbf{I}$, the synthetic data vector $\mathbf{y}$ has the desired covariance $\langle \mathbf{y}\mathbf{y}^\mathrm{T} \rangle = \mathbf{L}\mathbf{x}\mathbf{x}^\mathrm{T}\mathbf{L}^\mathrm{T} = \mathbf{L}\mathbf{L}^\mathrm{T} = \mathbf{C}$.

We generate 10 realizations of such synthetic data for each SWH threshold using $\omega_0/2\pi = 5.5 \times 10^{-3}$ cpd and $A = 74.7$ m^2 cpd^{-1}, the parameter inferred from altimetry. We then apply the same interpolation and spectral analysis as used for the real GPS data to each realization of synthetic data, then we average over the realizations. The result shows that the estimated spectra closely approximate the true spectrum for all SWH thresholds at the frequencies of interest, with only a modest underestimate in spectral level for the most stringent threshold (Fig. A1b). This confirms that our interpolation and spectral estimation method is robust to the gaps introduced by high sea states.

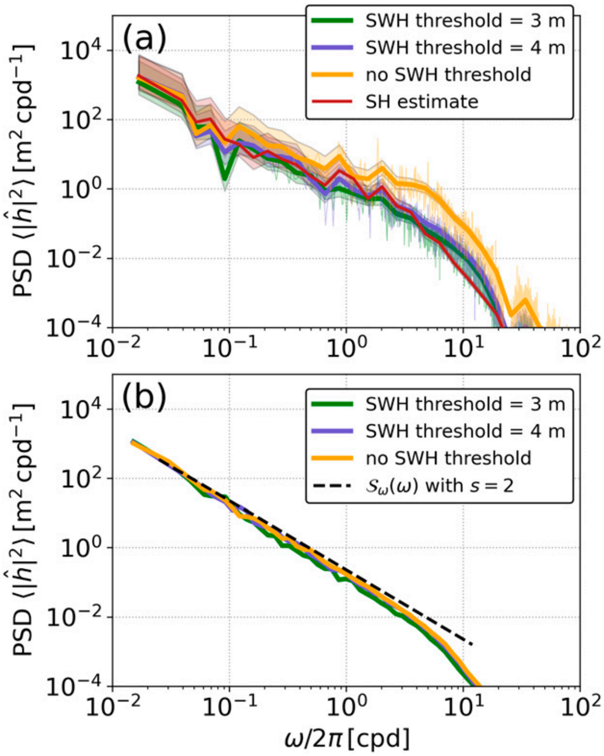

FIG. A1. Sensitivity of spectral estimates to high sea states and data gaps. (a) Frequency spectra of SSH variance obtained from the northern GPS buoy for three different significant wave height (SWH) thresholds (green, blue, yellow) and as estimated from bottom pressure plus steric height (SH; red). Dashed lines show estimates with tides, solid lines show estimates with the tidal signal removed prior to the spectral estimation. (b) Spectra estimated from synthetic data with known covariance (A2), generated at the same time stamps as the observations with different SWH thresholds applied. The interpolation and spectral analysis applied to the synthetic data is the same as that applied to the real GPS data. The true spectrum is shown by the dashed black line.

The main difference between the three spectra computed from the GPS buoys time series (Fig. A1a) is seen at superinertial frequencies (that are not of primary interest in this study): the larger the threshold, the larger the apparent SSH variance. This difference could be the result of a response to wind forcing if this frequency range is dominated by internal waves. It could also be caused by high-frequency GPS errors due to high sea states, however, thus resulting in a spurious increase of the SSH variance. Both the GPS errors and relationship between the signal and wind warrant further exploration but are beyond the scope of the present study.

It is well established that precise GPS time series contain errors capable of masking geophysical signals. Prevailing interpretations from the evaluation of terrestrial GPS data are expected to apply equally to data collected on the ocean. Errors in long time series of routine (daily) station position

TABLE A1. Tandem solution strategy for GPS buoys: nominal vs perturbed. GPS orbits and clocks are fixed, as in precise point positioning, but observations from both buoys are processed together to allow additional constraints.

Background model	Nominal	Perturbed
GPS orbit and clock product	JPL final	JPL rapid (next day)
Buoy attitude	From onboard sensor	Static, zenith pointing
Water line offset[a]	1.0668 m	0 m
Antenna phase center and variations	Empirical[b]	None
Antenna group-delay variations	Empirical[b]	None
Dry troposphere mapping function	VMF1 (Boehm et al. 2006)	NMF (Niell 1996)
Wet troposphere mapping function	VMF1	NMF
Zenith dry troposphere delay	VMF1	VMF1
Zenith wet troposphere delay	From low-rate estimate[c]	From low-rate estimate[c]
Elevation-dependent observation weight	$\sigma = \sigma_o$ (flat)	$\sigma = \sqrt{\sigma_o/\sin^2(\varepsilon)}$
Postfit edit threshold (LC)	2.5 cm	5.0 cm
Elevation cutoff (antenna frame)	10°	10°
Elevation cutoff (local horizon)	7°	10°
Earth tide and pole tide	IERS (Petit and Luzum 2010)	IERS
Ocean load tide	FES2004 (Lyard et al. 2006)	FES2004

SSH corrections	Nominal	Perturbed
Geoid variation	Sandwell[d]	CLS2021
Mooring line tension	2.54 cm displacement per 105 lbf[e]	Use avg for 2 buoys
Sea state bias[f]	1.8% of SWH	1.6% of SWH

Estimated parameter	Parameterization	σ	σ_p
Position	White noise: 1-s updates	100 m	100 m
Clock offset	White noise: 1-s updates	1 s	1 s
Carrier-phase biases	White noise update at breaks[g]	3×10^5 km	3×10^5 km
Zenith wet troposphere[h]	Bias per solution arc	50 cm	—

Tracking data	σ_o	Rate
Ionosphere-free carrier phase: LC = 2.54(L1) − 1.54(L2)	1 cm	1 s
Ionosphere-free pseudorange: PC = 2.54(P1) − 1.54(P2)	100 cm	1 s

[a] Vertical offset to GPS antenna reference point in calm waters.
[b] Estimated from data, with a priori from NGS model for SEPPOLANT_X_MF (https://geodesy.noaa.gov/ANTCAL/).
[c] From low-rate (5-min) GPS solutions, with common (between buoys) zenith wet troposphere estimated as random walk (σ_p = 10 mm $\mathrm{h}^{-1/2}$).
[d] CLS MSS (Schaeffer et al. 2012) v. 2019, tuned with data from Sentinel-3 (D. Sandwell 2020, personal communication).
[e] From load cell in pounds force (lbf); displacement estimate from C. Meinig (2018, personal communication).
[f] Empirical estimate to account for systematic impacts from waves on GPS technique.
[g] Ambiguities resolved using product widelanes (Bertiger et al. 2010) and directly on double differences between buoys.
[h] For perturbed solution only, as coarse correction to nominal from low-rate estimate.

estimates are commonly described as a combination of white (0 slope) and flicker (−1 slope) noise (Zhang et al. 1997; Mao et al. 1999; Williams et al. 2004) over periods ranging from 2 days to a few years. High-rate solutions, used for example in studying earthquakes, show similar behavior at higher frequencies (Bock et al. 2000; Langbein and Bock 2004), where random walk (−2 slope) noise has also been noted (Itoh and Aoki 2022). Also prominent are discrete harmonic signals linked to overtones of the GPS draconitic year (~350 days) (Ray et al. 2008) and to the sidereal daily repeat of the GPS constellation (Itoh and Aoki 2022). Potential sources of the GPS errors include uncompensated troposphere refraction and multipath, as well as monument instabilities and errors linked to uncertainty in the GPS satellite orbit and clock estimates.

Confounding the situation for the buoys are errors linked to the open-ocean environment, notably from waves, which cause turbulent platform motions and also impact visibility of GPS satellites at low elevations depending on the prevailing SWH. Reconciling the position of the GPS antenna to the water line is a significant challenge and involves not only corrections for the buoy attitude but also for variations in the mooring line tension (Zhou et al. 2020). Finally, the corrections applied to geodetic SSH, as measured by both GPS buoys and satellite altimetry, to yield dynamic height (corrected SSH) have errors which contribute to the spectra. These include corrections for the mean sea surface (from a model, see footnote in Table A1), which reflect primarily the variations in the marine geoid as the buoys drift within the watch circles, as well as the inverted barometer (from reanalysis).

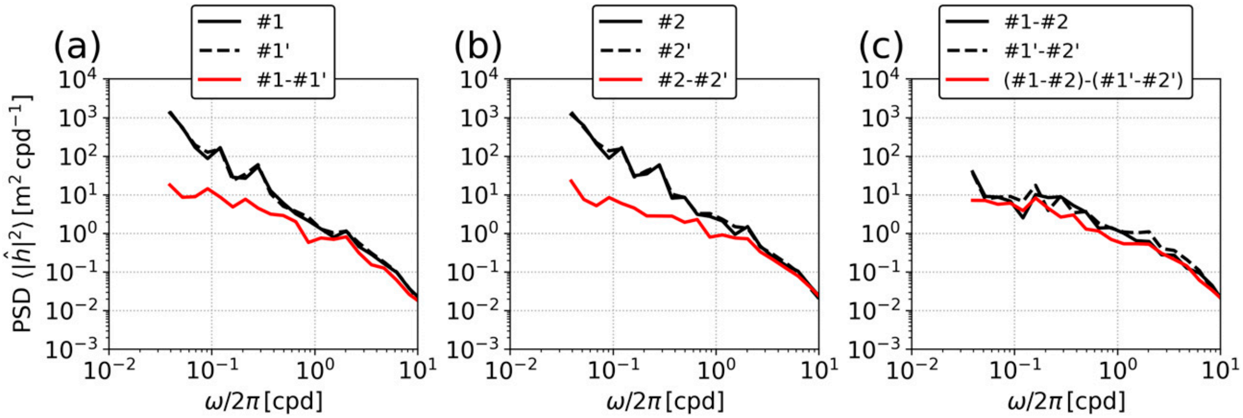

FIG. A2. Sensitivity of GPS-derived spectra to processing choices. (a) Spectrum of the nominal GPS buoy 1 time series used in this study (solid black) compared to the spectrum of the perturbed GPS solution (1′, dashed black) and the spectrum of the difference between the nominal time series and the perturbed solution (red). (b) As in (a), but for the GPS buoy 2. (c) As in (a), but for the difference between the two GPS time series and their associated perturbed solutions.

In face of these errors linked to the GPS technique (and SSH corrections), we need to confirm that the derived spectral estimates are dominated by meso- and submesoscale signals rather than these errors. To address this, we generated using the same GipsyX software as for the nominal solution (Bertiger et al. 2020) a perturbed GPS buoy solution intended to expose the errors in these novel GPS measurements of SSH. Details of the strategies underlying this perturbed (degraded) solution in comparison to the nominal strategy are provided in Table A1.

We conduct a sensitivity study by comparing the perturbed GPS solution and the nominal time series (i.e., the difference between the nominal and the perturbed solution is the estimate of the GPS error, see red lines in Fig. A2). Individual buoy spectra (Figs. A2a,b) are about an order of magnitude larger than the GPS error in the frequency range of interest ($\omega/2\pi < 1$ cpd), lending further confidence in the dataset. The error peak at the semidiurnal band could be due in part to errors in the modeling of the water line (from observations of mooring line tension) as the buoy shifts up and down in cadence with the predominant M_2 tide. The relative error on the difference spectrum is larger (Fig. A2c), but the signal remains at least twice the size of the perturbation error for most frequencies below 1 cpd. It should be kept in mind that we designed the perturbation primarily to give a proxy for the shape of the error spectrum, whereas the spectral amplitude is set by the intensity of the perturbation, which is here large on purpose. Actual errors are likely smaller.

REFERENCES

Arbic, B. K., R. B. Scott, G. R. Flierl, A. J. Morten, J. G. Richman, and J. F. Shriver, 2012: Nonlinear cascades of surface oceanic geostrophic kinetic energy in the frequency domain. *J. Phys. Oceanogr.*, **42**, 1577–1600, https://doi.org/10.1175/JPO-D-11-0151.1.

Babiano, A., C. Basdevant, and R. Sadourny, 1985: Structure functions and dispersion laws in two-dimensional turbulence. *J. Atmos. Sci.*, **42**, 941–949, https://doi.org/10.1175/1520-0469(1985)042<0941:SFADLI>2.0.CO;2.

Balwada, D., K. S. Smith, and R. Abernathey, 2018: Submesoscale vertical velocities enhance tracer subduction in an idealized Antarctic Circumpolar Current. *Geophys. Res. Lett.*, **45**, 9790–9802, https://doi.org/10.1029/2018GL079244.

Bertiger, W., S. D. Desai, B. Haines, N. Harvey, A. W. Moore, S. Owen, and J. P. Weiss, 2010: Single receiver phase ambiguity resolution with GPS data. *J. Geod.*, **84**, 327–337, https://doi.org/10.1007/s00190-010-0371-9.

——, and Coauthors, 2020: GipsyX/RTGx, a new tool set for space geodetic operations and research. *Adv. Space Res.*, **66**, 469–489, https://doi.org/10.1016/j.asr.2020.04.015.

Boccaletti, G., R. Ferrari, and B. Fox-Kemper, 2007: Mixed layer instabilities and restratification. *J. Phys. Oceanogr.*, **37**, 2228–2250, https://doi.org/10.1175/JPO3101.1.

Bock, Y., R. M. Nikolaidis, P. J. de Jonge, and M. Bevis, 2000: Instantaneous geodetic positioning at medium distances with the global positioning system. *J. Geophys. Res.*, **105**, 28 223–28 253, https://doi.org/10.1029/2000JB900268.

Boehm, J., A. Niell, P. Tregoning, and H. Schuh, 2006: Global Mapping Function (GMF): A new empirical mapping function based on numerical weather model data. *Geophys. Res. Lett.*, **33**, L07304, https://doi.org/10.1029/2005GL025546.

Brannigan, L., D. P. Marshall, A. C. Naveira Garabato, A. J. G. Nurser, and J. Kaiser, 2017: Submesoscale instabilities in mesoscale eddies. *J. Phys. Oceanogr.*, **47**, 3061–3085, https://doi.org/10.1175/JPO-D-16-0178.1.

Buckingham, C. E., and Coauthors, 2016: Seasonality of submesoscale flows in the ocean surface boundary layer. *Geophys. Res. Lett.*, **43**, 2118–2126, https://doi.org/10.1002/2016GL068009.

Bühler, O., J. Callies, and R. Ferrari, 2014: Wave–vortex decomposition of one-dimensional ship-track data. *J. Fluid Mech.*, **756**, 1007–1026, https://doi.org/10.1017/jfm.2014.488.

Callies, J., and R. Ferrari, 2013: Interpreting energy and tracer spectra of upper-ocean turbulence in the submesoscale range (1–200 km). *J. Phys. Oceanogr.*, **43**, 2456–2474, https://doi.org/10.1175/JPO-D-13-063.1.

——, and W. Wu, 2019: Some expectations for submesoscale sea surface height variance spectra. *J. Phys. Oceanogr.*, **49**, 2271–2289, https://doi.org/10.1175/JPO-D-18-0272.1.

——, R. Ferrari, J. M. Klymak, and J. Gula, 2015: Seasonality in submesoscale turbulence. *Nat. Commun.*, **6**, 6862, https://doi.org/10.1038/ncomms7862.

——, G. Flierl, R. Ferrari, and B. Fox-Kemper, 2016: The role of mixed-layer instabilities in submesoscale turbulence. *J. Fluid Mech.*, **788**, 5–41, https://doi.org/10.1017/jfm.2015.700.

——, R. Barkan, and A. C. Naveira Garabato, 2020: Time scales of submesoscale flow inferred from a mooring array. *J. Phys. Oceanogr.*, **50**, 1065–1086, https://doi.org/10.1175/JPO-D-19-0254.1.

Capet, X., J. C. McWilliams, M. J. Molemaker, and A. F. Shchepetkin, 2008: Mesoscale to submesoscale transition in the California Current system. Part I: Flow structure, eddy flux, and observational tests. *J. Phys. Oceanogr.*, **38**, 29–43, https://doi.org/10.1175/2007JPO3671.1.

Charney, J. G., 1971: Geostrophic turbulence. *J. Atmos. Sci.*, **28**, 1087–1095, https://doi.org/10.1175/1520-0469(1971)028<1087:GT>2.0.CO;2.

Chelton, D. B., M. G. Schlax, R. M. Samelson, J. T. Farrar, M. J. Molemaker, J. C. McWilliams, and J. Gula, 2019: Prospects for future satellite estimation of small-scale variability of ocean surface velocity and vorticity. *Prog. Oceanogr.*, **173**, 256–350, https://doi.org/10.1016/j.pocean.2018.10.012.

Chen, S., and B. Qiu, 2021: Sea surface height variability in the 30–120 km wavelength band from altimetry along-track observations. *J. Geophys. Res. Oceans*, **126**, e2021JC017284, https://doi.org/10.1029/2021JC017284.

Chereskin, T. K., C. B. Rocha, S. T. Gille, D. Menemenlis, and M. Passaro, 2019: Characterizing the transition from balanced to unbalanced motions in the Southern California Current. *J. Geophys. Res. Oceans*, **124**, 2088–2109, https://doi.org/10.1029/2018JC014583.

de Marez, C., T. Meunier, M. Morvan, P. L'Hégaret, and X. Carton, 2020: Study of the stability of a large realistic cyclonic eddy. *Ocean Modell.*, **146**, 101540, https://doi.org/10.1016/j.ocemod.2019.101540.

Desai, S., 2018: Surface Water and Ocean Topography Mission (SWOT) Project Science Requirements Document. NASA Tech. Rep. JPL D-61923, 29 pp. https://swot.jpl.nasa.gov/system/documents/files/2176_2176_D-61923_SRD_Rev_B_20181113.pdf.

Elipot, S., and S. T. Gille, 2009: Estimates of wind energy input to the Ekman layer in the Southern Ocean from surface drifter data. *J. Geophys. Res.*, **114**, C06003, https://doi.org/10.1029/2008JC005170.

Ferrari, R., and C. Wunsch, 2010: The distribution of eddy kinetic and potential energies in the global ocean. *Tellus*, **62A**, 92–108, https://doi.org/10.1111/j.1600-0870.2009.00432.x.

Fox-Kemper, B., R. Ferrari, and R. Hallberg, 2008: Parameterization of mixed layer eddies. Part I: Theory and diagnosis. *J. Phys. Oceanogr.*, **38**, 1145–1165, https://doi.org/10.1175/2007JPO3792.1.

Freilich, M., and A. Mahadevan, 2021: Coherent pathways for subduction from the surface mixed layer at ocean fronts. *J. Geophys. Res. Oceans*, **126**, e2020JC017042, https://doi.org/10.1029/2020JC017042.

Fu, L.-L., and R. Ferrari, 2008: Observing oceanic submesoscale processes from space. *Eos, Trans. Amer. Geophys. Union*, **89**, 488, https://doi.org/10.1029/2008EO480003.

Fund, F., F. Perosanz, L. Testut, and S. Loyer, 2013: An integer precise point positioning technique for sea surface observations using a GPS buoy. *Adv. Space Res.*, **51**, 1311–1322, https://doi.org/10.1016/j.asr.2012.09.028.

Garrett, C., and W. Munk, 1972: Space-time scales of internal waves. *Geophys. Fluid Dyn.*, **3**, 225–264, https://doi.org/10.1080/03091927208236082.

Gill, A. E., and P. P. Niiler, 1973: The theory of the seasonal variability in the ocean. *Deep-Sea Res. Oceanogr. Abstr.*, **20**, 141–177, https://doi.org/10.1016/0011-7471(73)90049-1.

Haines, B., S. Desai, C. Meinig, and S. Stalin, 2017: CALVAL of the SWOT SSH spectrum: Moored GPS buoy approach. *SWOT Second Science Team Meeting*, Toulouse, France, NASA, 11 pp., https://hdl.handle.net/2014/48164.

——, ——, A. Dodge, B. Leben, M. Shannon, C. Meinig, and S. Stalin, 2019: The Harvest experiment: New results from the platform and moored GPS buoys. *Ocean Surface Topography Science Team Meeting*, Chicago, IL, NASA, 20 pp., https://trs.jpl.nasa.gov/handle/2014/51953.

Ioannou, A., A. Stegner, B. Le Vu, I. Taupier-Letage, and S. Speich, 2017: Dynamical evolution of intense Ierapetra eddies on a 22 year long period. *J. Geophys. Res. Oceans*, **122**, 9276–9298, https://doi.org/10.1002/2017JC013158.

Itoh, Y., and Y. Aoki, 2022: On the performance of position-domain sidereal filter for 30-s kinematic GPS to mitigate multipath errors. *Earth Planets Space*, **74**, 23, https://doi.org/10.1186/s40623-022-01584-8.

Jacobs, G. A., G. H. Born, M. E. Parke, and P. C. Allen, 1992: The global structure of the annual and semiannual sea surface height variability from Geosat altimeter data. *J. Geophys. Res.*, **97**, 17 813–17 828, https://doi.org/10.1029/92JC01708.

Kamphaus, R., 2014: HA 14-03 WHOI Hawaii ocean time-series station (WHOTS). Project Number HA 14-03, 33 pp., https://repository.library.noaa.gov/view/noaa/16540.

Klein, P., B. L. Hua, G. Lapeyre, X. Capet, S. Le Gentil, and H. Sasaki, 2008: Upper ocean turbulence from high-resolution 3D simulations. *J. Phys. Oceanogr.*, **38**, 1748–1763, https://doi.org/10.1175/2007JPO3773.1.

Langbein, J., and Y. Bock, 2004: High-rate real-time GPS network at Parkfield: Utility for detecting fault slip and seismic displacements. *Geophys. Res. Lett.*, **31**, L15S20, https://doi.org/10.1029/2003GL019408.

Lawrence, A., and J. Callies, 2022: Seasonality and spatial dependence of mesoscale and submesoscale ocean currents from along-track satellite altimetry. *J. Phys. Oceanogr.*, **52**, 2069–2089, https://doi.org/10.1175/JPO-D-22-0007.1.

Le Traon, P.-Y., G. Dibarboure, G. Jacobs, M. Martin, E. Rémy, and A. Schiller, 2017: Use of satellite altimetry for operational oceanography. *Satellite Altimetry over Oceans and Land Surfaces*, CRC Press, 581–608.

Lévy, M., P. J. S. Franks, and K. S. Smith, 2018: The role of submesoscale currents in structuring marine ecosystems. *Nat. Commun.*, **9**, 4758, https://doi.org/10.1038/s41467-018-07059-3.

Lyard, F., F. Levevre, T. Letellier, and O. Francis, 2006: Modelling the global ocean tides: Modern insights from FES2004. *Ocean Dyn.*, **56**, 394–415, https://doi.org/10.1007/s10236-006-0086-x.

Mao, A., C. G. A. Harrison, and T. H. Dixon, 1999: Noise in GPS coordinate time series. *J. Geophys. Res.*, **104**, 2797–2816, https://doi.org/10.1029/1998JB900033.

McWilliams, J. C., 2016: Submesoscale currents in the ocean. *Proc. Roy. Soc.*, **472A**, 20160117, https://doi.org/10.1098/rspa.2016.0117.

Morrow, R., and Coauthors, 2019: Global observations of fine-scale ocean surface topography with the Surface Water and Ocean Topography (SWOT) mission. *Front. Mar. Sci.*, **6**, 232, https://doi.org/10.3389/fmars.2019.00232.

Niell, A. E., 1996: Global mapping functions for the atmosphere delay at radio wavelengths. *J. Geophys. Res.*, **101**, 3227–3246, https://doi.org/10.1029/95JB03048.

Penna, N. T., M. A. Morales Maqueda, I. Martin, J. Guo, and P. R. Foden, 2018: Sea surface height measurement using a GNSS wave glider. *Geophys. Res. Lett.*, **45**, 5609–5616, https://doi.org/10.1029/2018GL077950.

Percival, D. B., and A. T. Walden, 1993: *Spectral Analysis for Physical Applications*. Cambridge University Press, 583 pp.

Petit, G., and B. Luzum, 2010: IERS conventions (2010). IERS Tech. Note 36, 179 pp., https://iers-conventions.obspm.fr/content/tn36.pdf.

Qiu, B., T. Nakano, S. Chen, and P. Klein, 2017: Submesoscale transition from geostrophic flows to internal waves in the northwestern Pacific upper ocean. *Nat. Commun.*, **8**, 14055, https://doi.org/10.1038/ncomms14055.

Ray, J., Z. Altamimi, X. Collilieux, and T. van Dam, 2008: Anomalous harmonics in the spectra of GPS position estimates. *GPS Solutions*, **12**, 55–64, https://doi.org/10.1007/s10291-007-0067-7.

Ray, R. D., and E. D. Zaron, 2016: M_2 internal tides and their observed wavenumber spectra from satellite altimetry. *J. Phys. Oceanogr.*, **46**, 3–22, https://doi.org/10.1175/JPO-D-15-0065.1.

Rocha, C. B., T. K. Chereskin, S. T. Gille, and D. Menemenlis, 2016: Mesoscale to submesoscale wavenumber spectra in Drake Passage. *J. Phys. Oceanogr.*, **46**, 601–620, https://doi.org/10.1175/JPO-D-15-0087.1.

Rodríguez, E., M. Bourassa, D. Chelton, J. Thomas Farrar, D. Long, D. Perkovic-Martin, and R. Samelson, 2019: The winds and currents mission concept. *Front. Mar. Sci.*, **6**, 438, https://doi.org/10.3389/fmars.2019.00438.

Sasaki, H., P. Klein, B. Qiu, and Y. Sasai, 2014: Impact of oceanic-scale interactions on the seasonal modulation of ocean dynamics by the atmosphere. *Nat. Commun.*, **5**, 5636, https://doi.org/10.1038/ncomms6636.

Schaeffer, P., Y. Faugére, J. F. Legeais, A. Ollivier, T. Guinle, and N. Picot, 2012: The CNES CLS11 global mean sea surface computed from 16 years of satellite altimeter data. *Mar. Geod.*, **35** (Suppl. 1), 3–19, https://doi.org/10.1080/01490419.2012.718231.

Schlax, M. G., and D. B. Chelton, 1994a: Aliased tidal errors in TOPEX/POSEIDON sea surface height data. *J. Geophys. Res.*, **99**, 24 761–24 775, https://doi.org/10.1029/94JC01925.

——, and ——, 1994b: Detecting aliased tidal errors in altimeter height measurements. *J. Geophys. Res.*, **99**, 12 603–12 612, https://doi.org/10.1029/94JC00568.

Sérazin, G., F. Marin, L. Gourdeau, S. Cravatte, R. Morrow, and M.-L. Dabat, 2020: Scale-dependent analysis of in situ observations in the mesoscale to submesoscale range around New Caledonia. *Ocean Sci.*, **16**, 907–925, https://doi.org/10.5194/os-16-907-2020.

Shcherbina, A. Y., E. A. D'Asaro, C. M. Lee, J. M. Klymak, M. J. Molemaker, and J. C. McWilliams, 2013: Statistics of vertical vorticity, divergence, and strain in a developed submesoscale turbulence field. *Geophys. Res. Lett.*, **40**, 4706–4711, https://doi.org/10.1002/grl.50919.

Soares, S. M., S. T. Gille, T. K. Chereskin, E. Firing, J. Hummon, and C. B. Rocha, 2022: Transition from balanced to unbalanced motion in the Eastern Tropical Pacific. *J. Phys. Oceanogr.*, **52**, 1775–1795, https://doi.org/10.1175/JPO-D-21-0139.1.

Stammer, D., 1997: Global characteristics of ocean variability estimated from regional TOPEX/POSEIDON altimeter measurements. *J. Phys. Oceanogr.*, **27**, 1743–1769, https://doi.org/10.1175/1520-0485(1997)027<1743:GCOOVE>2.0.CO;2.

Su, Z., J. Wang, P. Klein, A. F. Thompson, and D. Menemenlis, 2018: Ocean submesoscales as a key component of the global heat budget. *Nat. Commun.*, **9**, 775, https://doi.org/10.1038/s41467-018-02983-w.

Taylor, G. I., 1938: The spectrum of turbulence. *Proc. Roy. Soc.*, **164A**, 476–490, https://doi.org/10.1098/rspa.1938.0032.

Taylor, J. R., and A. F. Thompson, 2023: Submesoscale dynamics in the upper ocean. *Annu. Rev. Fluid Mech.*, **55**, 103–127, https://doi.org/10.1146/annurev-fluid-031422-095147.

——, S. Bachman, M. Stamper, P. Hosegood, K. Adams, J.-B. Sallee, and R. Torres, 2018: Submesoscale rossby waves on the Antarctic circumpolar current. *Sci. Adv.*, **4**, eaao2824, https://doi.org/10.1126/sciadv.aao2824.

Tennekes, H., and J. L. Lumley, 1972: *A First Course in Turbulence*. MIT Press, 320 pp.

Thomson, R. E., and W. J. Emery, 2014: *Data Analysis Methods in Physical Oceanography*. Newnes, 728 pp.

Vergara, O., R. Morrow, I. Pujol, G. Dibarboure, and C. Ubelmann, 2019: Revised global wave number spectra from recent altimeter observations. *J. Geophys. Res. Oceans*, **124**, 3523–3537, https://doi.org/10.1029/2018JC014844.

Villas Bôas, A. B., L. Lenain, B. D. Cornuelle, S. T. Gille, and M. R. Mazloff, 2022: A broadband view of the sea surface height wavenumber spectrum. *Geophys. Res. Lett.*, **49**, e2021GL096699, https://doi.org/10.1029/2021GL096699.

Wang, J., and Coauthors, 2022: On the development of SWOT in-situ calibration/validation for short-wavelength ocean topography. *J. Atmos. Oceanic Technol.*, **39**, 595–617, https://doi.org/10.1175/JTECH-D-21-0039.1.

Weller, R. A., 2015: Variability and trends in surface meteorology and air–sea fluxes at a site off northern Chile. *J. Climate*, **28**, 3004–3023, https://doi.org/10.1175/JCLI-D-14-00591.1.

Williams, S. D. P., Y. Bock, P. Fang, P. Jamason, R. M. Nikolaidis, L. Prawirodirdjo, M. Miller, and D. J. Johnson, 2004: Error analysis of continuous GPS position time series. *J. Geophys. Res.*, **109**, B03412, https://doi.org/10.1029/2003JB002741.

Wortham, C., and C. Wunsch, 2014: A multidimensional spectral description of ocean variability. *J. Phys. Oceanogr.*, **44**, 944–966, https://doi.org/10.1175/JPO-D-13-0113.1.

Wunsch, C., 2006: *Discrete Inverse and State Estimation Problems.* Cambridge University Press, 371 pp.

Xu, Y., and L.-L. Fu, 2011: Global variability of the wavenumber spectrum of oceanic mesoscale turbulence. *J. Phys. Oceanogr.*, **41**, 802–809, https://doi.org/10.1175/2010JPO4558.1.

——, and ——, 2012: The effects of altimeter instrument noise on the estimation of the wavenumber spectrum of sea surface height. *J. Phys. Oceanogr.*, **42**, 2229–2233, https://doi.org/10.1175/JPO-D-12-0106.1.

Zhang, J., Y. Bock, H. Johnson, P. Fang, S. Williams, J. Genrich, S. Wdowinski, and J. Behr, 1997: Southern California permanent GPS geodetic array: Error analysis of daily position estimates and site velocities. *J. Geophys. Res.*, **102**, 18 035–18 055, https://doi.org/10.1029/97JB01380.

Zhao, Z., M. H. Alford, J. B. Girton, L. Rainville, and H. L. Simmons, 2016: Global observations of open-ocean mode-1 M_2 internal tides. *J. Phys. Oceanogr.*, **46**, 1657–1684, https://doi.org/10.1175/JPO-D-15-0105.1.

Zhou, B., C. Watson, B. Legresy, M. A. King, J. Beardsley, and A. Deane, 2020: GNSS/INS-equipped buoys for altimetry validation: Lessons learnt and new directions from the Bass Strait validation facility. *Remote Sens.*, **12**, 3001, https://doi.org/10.3390/rs12183001.